

Optical study on intrinsic exciton states in high-quality $\text{CH}_3\text{NH}_3\text{PbBr}_3$ single crystalsT. Thu Ha Do,¹ A. Granados del Águila,¹ Chao Cui,² Jun Xing,¹ Zhijun Ning,^{2,*} and Qihua Xiong^{1,3,†}¹*Division of Physics and Applied Physics, School of Physical and Mathematical Sciences, Nanyang Technological University, 637371, Singapore*²*School of Physical Science and Technology, ShanghaiTech University, Shanghai, 201210, China*³*NOVITAS, Nanoelectronics Centre of Excellence, School of Electrical and Electronic Engineering, Nanyang Technological University, 639798, Singapore*

(Received 3 March 2017; revised manuscript received 16 June 2017; published 24 August 2017)

Organolead halide perovskites have emerged as potential building blocks for photovoltaic and optoelectronic devices. Yet the underlying fundamental physics is not well understood. There is lack of agreement on the electronic band structures and binding energies of coupled electron-hole pairs (excitons), which drive the photophysical processes. In this work, we conducted temperature-dependent reflectance and photoluminescence experiments on high-quality $\text{CH}_3\text{NH}_3\text{PbBr}_3$ single crystals. Two direct optical transitions corresponding to intrinsic free-excitons are clearly resolved, showing excellent consistence between the low-temperature ($T = 10$ K) reflectance and photoluminescence spectra. Remarkably, the excitons have different binding energies and behave oppositely with temperature, suggesting distinctive origins. Moreover, the asymmetric photoluminescence profile is counterintuitively dominated by the high-energy exciton that is explained by a long relaxation time between levels and by the favorable generation rate of electron-hole pairs at the high-energy band. Our study opens access to the intrinsic properties of $\text{CH}_3\text{NH}_3\text{PbBr}_3$ and sheds light to reconcile the large range of binding energies reported on these emergent direct band-gap semiconductors.

DOI: [10.1103/PhysRevB.96.075308](https://doi.org/10.1103/PhysRevB.96.075308)**I. INTRODUCTION**

Lead halide perovskite (LHP) semiconductors have had a tremendous impact, in a short period of time, in several optoelectronic applications such as efficient light-energy harvesting in low-cost solar cells [1–3], light-emitting devices [4–8], nanolasers [9–11], photodetectors [12–14], and optical refrigerators [15]. Due to their direct band gap and large interband dipole moment, LHPs generally exhibit strong photoluminescence (PL) whose emission wavelength is tunable from near-ultraviolet to near-infrared regions, by varying the chemical constituents or by alloying the halide elements [9,10,16–21]. Despite the disproportionate improvement on low-cost synthesis and perovskite-based devices, the fundamental physics underlying such excellent performances has just started to attract attention.

The chemical structure of LHP semiconductors is YMZ_3 , where Y is methylammonium ($\text{CH}_3\text{NH}_3^+ = \text{MA}^+$), formamidinium ($\text{CH}(\text{NH}_2)_2^+ = \text{FA}^+$), or cesium cation (Cs^+); M is lead cation (Pb^{2+}); and Z is iodide (I^-), bromide (Br^-), or chloride anion (Cl^-). These perovskite compounds share similar electronic structures [22–25]. They exist in different crystal phases, depending on external conditions such as pressure or temperature [26–28]. For instance, $\text{CH}_3\text{NH}_3\text{PbBr}_3$ transforms from the orthorhombic phase at below 150 K to the tetragonal phase at 150 K to 240 K and exists in the cubic phase at above 240 K [29]. The phase transitions can cause abrupt changes in band gaps as well as in electronic band structures. The direct gaps of $\text{CH}_3\text{NH}_3\text{PbZ}_3$ are located at the Γ and R points in the Brillouin zone for orthorhombic and cubic phases, respectively [23,30,31]. Moreover, large spin-orbit splitting

is expected in heavy-metal-containing semiconductors such as Pb [32–35]. A giant Rashba effect has been predicted theoretically [36,37] and recently observed experimentally [38]. In addition, crystal field asymmetries and electron-hole exchange interactions [39] add to the plethora of physical parameters that need to be explored to fully understand the electronic energy landscape and optical transitions of these emergent semiconductors.

In addition to theoretical studies, a number of optical experiments have been conducted leading to many unsolved questions, because the observations seem to contradict each other. Particularly, the dominant process governing the optical responses of $\text{CH}_3\text{NH}_3\text{PbZ}_3$ at room temperature remains controversial between free carriers and excitons [19,39–46]. Regarding weakly or tightly bound pairs, knowledge of the binding energies among electrons and holes paves the way to understand the photophysics of the materials and, therefore, is a critical factor for device design and operation.

It has been argued that the semiconducting LHP family has relatively simple band structures. Despite different measurements, including magneto-absorption and temperature-dependent and optical absorption, exciton binding energies are reported over a wide range: 2–55 meV for $\text{CH}_3\text{NH}_3\text{PbI}_3$ [40,41], 15–100 meV for $\text{CH}_3\text{NH}_3\text{PbBr}_3$ [19,39,42–46], and 50 meV for $\text{CH}_3\text{NH}_3\text{PbCl}_3$ [19]. However, most of these studies have been carried out in chemically processed thin films, which are normally affected by defects, impurities, and poor crystallinity, and thus, sample-to-sample variation prevails. Therefore, optical studies on high-quality crystals are urged to clarify the photophysics and energy structures of LHPs.

In this work, we systematically investigate the intrinsic optical properties of high-quality $\text{CH}_3\text{NH}_3\text{PbBr}_3$ single crystals using temperature-dependent reflectance and photoluminescence spectroscopy techniques. We show that the optical responses of the $\text{CH}_3\text{NH}_3\text{PbBr}_3$ single crystal at low and high

*ningzhj@shanghaitech.edu.cn

†qihua@ntu.edu.sg

temperatures are governed by two different classes of free excitons with distinct binding energies: one of them tends to dissociate, while the other remains pronounced near room temperature. Additionally, the photoluminescence spectrum shows a nontrivial and counterintuitive intensity profile that is ascribed to the long relaxation time between excitonic levels and the preferential creation of electron-hole pairs at the high-energy band. We show that light emission of the $\text{CH}_3\text{NH}_3\text{PbBr}_3$ single crystal is a complex process. Our results are in line with reconciling the wide range of exciton binding energies found in lead halide $\text{CH}_3\text{NH}_3\text{PbBr}_3$ and provide a direct approach to investigating excitonic properties of other perovskite semiconductors.

II. EXPERIMENTAL DETAILS

A. Synthesis of $\text{CH}_3\text{NH}_3\text{PbBr}_3$ single crystal

The $\text{CH}_3\text{NH}_3\text{PbBr}_3$ single crystal was prepared by inverse temperature crystallization with slight modifications [47]. One molar (1.0 M) PbBr_2 and 1.0 M $\text{CH}_3\text{NH}_3\text{Br}$ (1:1 molar ratio) were dissolved in dimethylformamide at room temperature and then filtered by a $0.22\text{-}\mu\text{m}$ polytetrafluoroethylene (PTFE) filter. The filtrate was heated to 80°C by using an oil bath and kept at this temperature for 3.5 h to allow crystal growth. The crystal was taken out from the precursor and subsequently washed with diethyl ether to remove the reagent residue on the crystal surface. In order to achieve the ideal size, a similar process was repeated one more time. In the second-round growth, the precursor concentration was increased to 1.2 M and the temperature was adjusted to 75°C . In comparison to reported methods, here we used diethyl ether as the solvent to wash the crystal surface. Owing the nonsolvent character of dimethyl ether for both PbBr_2 and $\text{CH}_3\text{NH}_3\text{Br}$, as well as its remarkably low boiling temperature, it can effectively reduce the interaction between the solvent and the perovskite crystal surface. This is important for prohibiting the formation of dangling-bond-related defects on the surface.

B. Steady-state reflectance and photoluminescence spectroscopy

Both the reflectance and the photoluminescence spectra were measured in a backscattering configuration. The excitation sources were switched between a broadband emission of a halogen lamp for reflectance experiments and the 457-nm line of an argon ion laser for steady-state PL measurements. The penetration depth of light into the sample, $\alpha^{-1}(\hbar\omega)$, is on the order of hundreds of nanometers for $\text{CH}_3\text{NH}_3\text{PbBr}_3$. The optical signals were collected through a microscope objective ($NA = 0.45$), dispersed by a single grating (300 g/mm) spectrometer and recorded by a nitrogen-cooled CCD camera. The millimeter-sized $\text{CH}_3\text{NH}_3\text{PbBr}_3$ single crystal was mounted in a cryostat fed by a continuous flow of liquid helium to control the temperature.

III. RESULTS AND DISCUSSION

A. Sample characterization and optical properties

Figure 1 shows the typical low-temperature ($T = 10\text{ K}$) reflectance (top black curve) and PL (bottom green curve) spectra measured on a high-quality $\text{CH}_3\text{NH}_3\text{PbBr}_3$ single

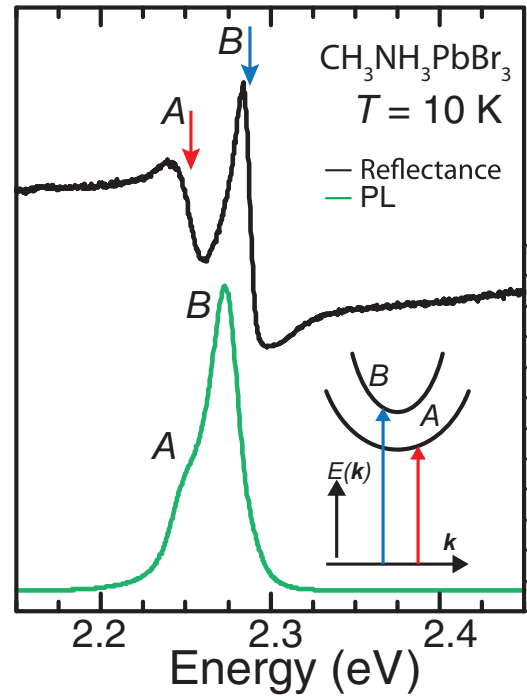


FIG. 1. Reflectance and PL spectra taken at low temperature ($T = 10\text{ K}$) on a high-quality $\text{CH}_3\text{NH}_3\text{PbBr}_3$ single crystal. Resonances A ($\sim 2.244\text{ eV}$) and B ($\sim 2.280\text{ eV}$) are clearly resolved in both reflectance (top black curve) and PL (bottom green curve) spectra. Inset: schematic energy diagram for direct optical transitions associated with intrinsic free excitons A and B given by red and blue arrows, respectively.

crystal. The sample has a millimeter size and provides flat surfaces for optical measurements (see Fig. S1 in Supplemental Material (SM) [48]). Single crystals can greatly reduce grain boundaries as well as trap states, which usually appear on polycrystalline thin films [47,49]. Indeed, evidenced in this work, no trap states have been detected in the optical spectra. Two sharp spectral resonances labeled A and B at energy positions of ~ 2.244 and $\sim 2.280\text{ eV}$, respectively, are clearly resolved in the reflectance spectrum corresponding to intrinsic free-exciton (X) transitions. Their derivativelike line shapes resemble direct excitonic features observed in the reflectance spectra of other direct band-gap semiconductors such as bulk GaAs [50] and ZnO [51], CdS thin films [52], and MoS_2 monolayers [53]. In such systems, an exciton is formed by an electron and a hole at the same k -point; therefore, it has zero wave vector (i.e., $\mathbf{K}_{\text{ex}} = \mathbf{k}_e - \mathbf{k}_h = \mathbf{0}$) [54]. A schematic energy diagram in exciton representation is shown in the inset of Fig. 1, where red and blue arrows denote the free-exciton transitions A and B, respectively.

The PL spectrum exhibits two discernible contributions. A high-energy structure ($\sim 2.270\text{ eV}$) originates from radiative recombination of free exciton B (X_B). At the low-energy side of X_B , a shoulder at approximately the same energy as the spectral resonance A in the reflectance spectrum can be distinguished, arising from radiative recombination of the low-energy exciton A (X_A). The good energy matching between the reflectance features and the emission peaks confirms the high quality of the investigated $\text{CH}_3\text{NH}_3\text{PbBr}_3$ single crystal.

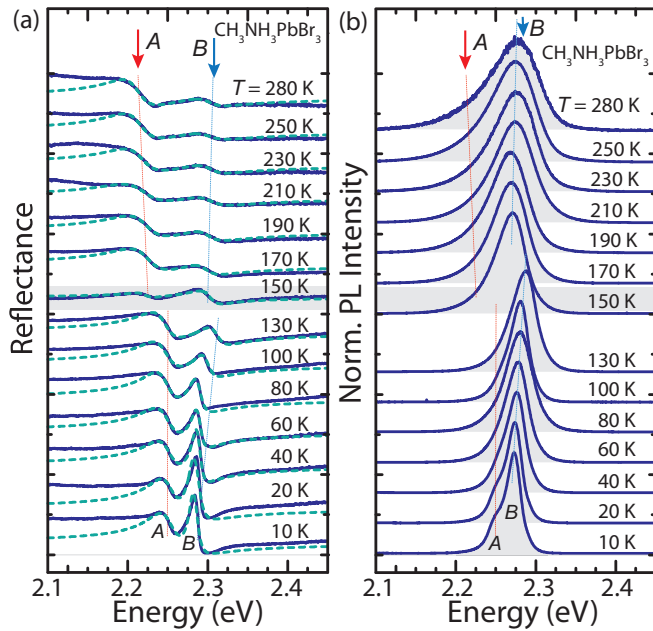


FIG. 2. (a) Reflectance spectra (blue solid lines) at selected temperatures from 10 K (bottom) to 280 K (top). The green dashed lines are fitting curves using two Lorentz oscillators (see text). The red and blue dotted lines are guidelines. The phase transition occurs at 150 K. The spectra are vertically shifted for clarity. (b) Same as panel (a) for PL spectra.

Noticeably, the high-energy X_B makes a contribution to the total PL intensity larger than that of the lowest-energy X_A .

B. Temperature-dependent reflectance and photoluminescence

To unravel the nature of the excitonic transitions, we monitored the changes in the reflectance and PL spectra upon temperature variations. Figures 2(a) and 2(b), respectively, show the reflectance and normalized PL spectra (blue solid lines) at selected temperatures from $T = 10$ K (bottom) to $T = 280$ K (top). The reflectance and PL spectra are vertically shifted for clarity. The $\text{CH}_3\text{NH}_3\text{PbBr}_3$ crystal undergoes a structural transition at $T \sim 150$ K, which is revealed in Figs. 2(a) and 2(b) as an abrupt change of the corresponding spectra. The phase-transition temperature agrees very well in both reflectance and PL experiments and also with previous reports in the $\text{CH}_3\text{NH}_3\text{PbBr}_3$ compound [42–44].

The behavior on temperature can be divided according to structural phases: orthorhombic ($T < 150$ K) and tetragonal-cubic ($T > 150$ K) phases. For simplicity, the low-temperature phase stands for the orthorhombic phase, whereas temperatures above 150 K we refer to as the high-temperature phase, and no distinction is made between cubic and tetragonal crystal structures. First, we describe the reflectance spectra [see Fig. 2(a)]. When increasing temperature from 10 K to 130 K (low-temperature phase), the spectral position of the high-energy exciton B shifts to higher energies (blue shift), its amplitude monotonically decreases, and its resonance linewidth increases. On the other hand, the low-energy exciton A hardly changes with temperature, and its energy position, amplitude, and linewidth are roughly constant. At the phase-

transition temperature ($T \sim 150$ K), the whole spectrum shifts to lower energies (red shift) and the reflectance amplitude of X_A suddenly drops, while that of X_B remains unperturbed by the phase change.

At the high-temperature phase, X_A recovers and exhibits a pronounced red-shift with increasing temperature, while its amplitude and linewidth are nearly constant. On the other hand, the excitonic transition X_B does not show significant energy changes, while its amplitude decreases and its linewidth increases with increasing temperature. It is worth noting that X_B is gradually smeared out and becomes hardly visible at elevated temperatures ($T \geq 230$ K); in contrast, X_A is still pronounced up to 280 K, indicating a large difference between binding energies (E_b) of excitons A and B . For the high-energy X_B , $E_{b,B}$ is smaller than or comparable to the thermal energy $k_B T$ at 230 K, where k_B is the Boltzmann constant ($k_B T \sim 20$ meV), whereas for the low-energy exciton A , $E_{b,A}$ is much larger than $k_B T$ at 280 K. In addition to the distinct binding energies, opposite energy shifts of the optical transitions with temperature also suggest different natures of free excitons A and B .

Figure 2(b) shows the normalized PL spectra (blue solid lines) at the same temperatures as in Fig. 2(a). Overall, the energy structure of the PL agrees well with the reflectance at all temperatures. First, contributions from the excitonic levels A and B can be distinguished at $T \leq 40$ K. The temperature rise causes a blue-shifted energy and a broader linewidth of X_B that obscures the contribution from X_A . Consequently, the low-energy feature X_A is no longer visible after $T \sim 40$ K. This trend remains until 130 K, just below the phase transition. The dominant contribution of the high-energy exciton B to the total PL intensity is nontrivial and is left for discussion.

At the high-temperature phase, the PL spectral position does not show significant variations, which is consistent with the almost unaffected reflectance in this temperature range [see Fig. 2(a)]. Although most of the emitted light arises from radiative recombination of free exciton B , the line shape remains asymmetric at the low-energy side of the PL spectrum that originates from free exciton A . This asymmetry increases with increasing temperature and is particularly prominent at $T \geq 200$ K. Moreover, the nonlinear power dependence of the integrated PL intensity at various temperatures (see Fig. S2 in SM [48]) confirms the existence of more than a single recombination process. Indeed, at this phase, multiple channels are expected to contribute to the PL spectral profile (see below).

We conducted similar reflectance and PL measurements on the second millimeter-sized and high-quality $\text{CH}_3\text{NH}_3\text{PbBr}_3$ single crystal which was fabricated independently by a different grower (see SM [48]). Also, two clear features are resolved in the reflectance spectra whose energies agree approximately well with resonances A and B . More importantly, they behave similarly to A and B with temperature (see Fig. S3 in SM [48]). The observation of similar behaviors in two independently grown samples provides strong evidence that A and B are intrinsic energy levels and play a decisive role in the electronic band structure of the $\text{CH}_3\text{NH}_3\text{PbBr}_3$ perovskite.

C. Resonant energies: Lorentz model

The experimental reflectance curves are fitted using the usual Fresnel expression for a semi-infinite medium

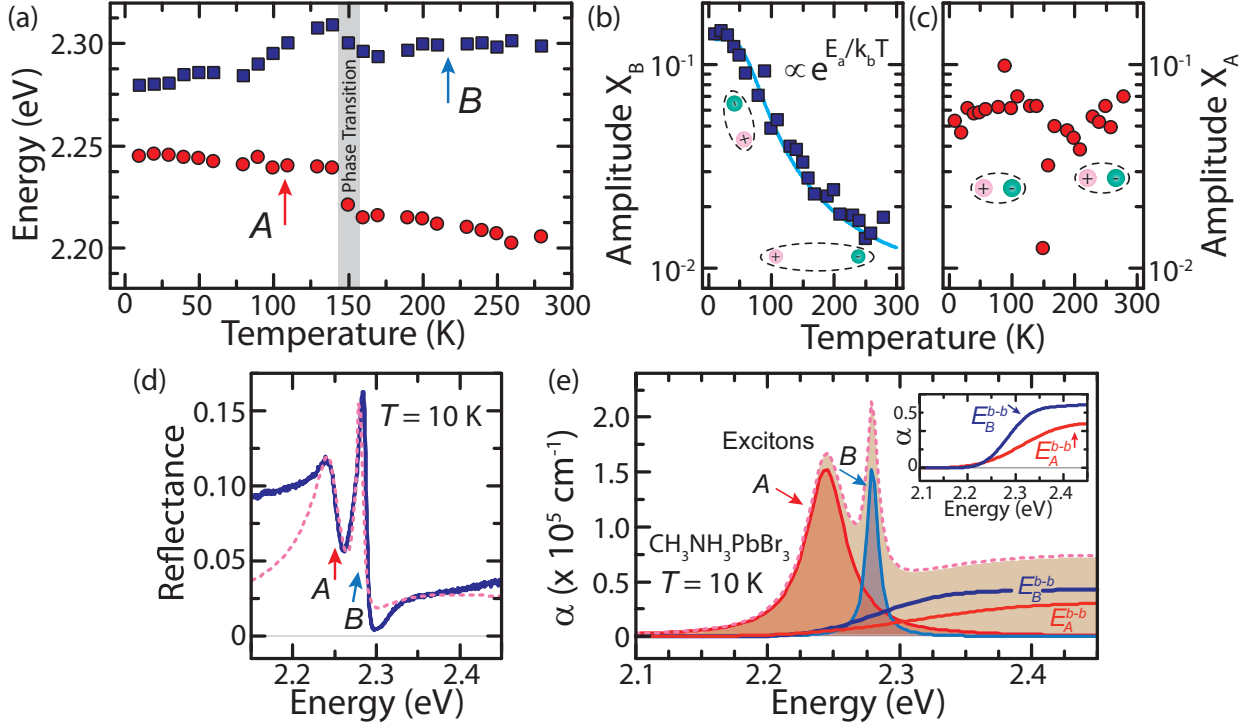


FIG. 3. (a) Resonance energies of free exciton A (red circles) and B (blue squares) versus temperature as extracted from the Lorentz model in Fig. 2(a). Error bars are comparable to the symbol sizes. (b) Reflectance amplitude of X_B (blue squares) as a function of temperature along with the fitting curve (cyan solid line) by an Arrhenius-like equation (see text). The cartoon illustrates a free exciton, where the distance (black dashed line) between electron (green circle) and hole (pink circle) displays the coupling strength of the exciton at low-temperature (tightly bound electron-hole pair) and high-temperature (weakly bound electron-hole pair) ranges. (c) Reflectance amplitude of X_A versus temperature with the same representation for excitons. The electron-hole pair is tightly bound at all temperatures, except at the phase-transition temperature $T \sim 150$ K. (d) Experimental reflectance at 10 K (blue solid line) along with the fitting curve (pink dotted line) derived from the combination of the Elliot theory and the Kramers-Kronig relationship (see text). (e) Total absorption coefficient as extracted from the model in panel (d) is shown by the pink dotted line. Different contributions include excitonic bands X_A and X_B (shaded area under the red and blue Lorentzian-shaped solid line, respectively) and the corresponding continuum bands E_A^{b-b} and E_B^{b-b} (areas under dark-orange and dark-blue solid lines, respectively).

given by [54]:

$$R(E) = \left| \frac{\tilde{n}(E) - 1}{\tilde{n}(E) + 1} \right|^2, \quad (1)$$

where E is the photon energy. The complex refractive index $\tilde{n}(E) = \sqrt{\tilde{\epsilon}(E)}$, where the complex dielectric function $\tilde{\epsilon}(E)$ can be expressed as a sum of oscillating dipoles A and B , according to the dipole oscillator model (Lorentz model) as follows [54]:

$$\tilde{\epsilon}(E) = \epsilon_\infty + \frac{\hbar^2 N e^2}{\epsilon_0 m_0} \sum_{j=A,B} \frac{F_j}{E_{0,j}^2 - E^2 - i\hbar\gamma_j E}, \quad (2)$$

where ϵ_∞ is the high-frequency dielectric constant, \hbar is the reduced Planck constant, N is the total number of oscillating dipoles, e is the free-electron charge, ϵ_0 is the electric permittivity of vacuum, m_0 is the free-electron rest mass, j ($j = A, B$) denotes the j -optical transition, $E_{0,j}$ is the j -resonance energy, $\hbar\gamma_j$ is the j -linewidth, and F_j is the j -oscillator strength that satisfies the sum rule $\sum_{j=A,B} F_j = 1$.

Combining Eqs. (1) and (2) results in the fitting curves shown by green dashed lines in Fig. 2(a). In the region of excitonic features A and B , excellent agreement is achieved

between the experimental reflectance and fitting curves at all temperatures. The extracted energies of X_A and X_B are plotted as a function of temperature in Fig. 3(a). The abrupt change due to the orthorhombic-tetragonal phase transition is highlighted at 150 K. Exciton B located at ~ 2.280 eV (at ~ 2.300 eV after 150 K) shows a blue shift with increasing temperature, which is opposite to the red shift of free excitons in conventional semiconductors such as GaAs [55], InP [56], and ZnS [57]. The unconventional shift of the optical resonance to high energies has been previously reported in Pb-based compounds [58] and is a common characteristic of lead halide perovskites [40,42,44,59].

The optical transition X_A occurs at a lower energy of ~ 2.244 eV (at ~ 2.220 eV after 150 K) and exhibits a *traditional* red shift with increasing temperature. The trend is more clearly seen after 150 K. The opposite energy responses of X_A and X_B to temperature are evidence for different origins of free excitons A and B .

D. Exciton binding energies

By applying the Lorentz model on the reflectance spectra [see Fig. 2(a)], the oscillator strengths of both excitonic transitions are found to be constant over the whole temperature

range, except for the discontinuity at the phase transition ($T \sim 150$ K) (see Fig. S4 in SM [48]). On the other hand, the amplitude of X_B decays exponentially as shown in Fig. 3(b), which can be well reproduced by an Arrhenius-like equation given by $A_R(T) = A_{0,R}[1 + C \exp(-E_a/k_B T)]^{-1}$ (cyan solid line). This function typically describes a dissociation process with activation energy E_a . In our case, it is equal to the exciton binding energy. Since the reflectance amplitude does not show any discontinuity even at the phase transition, the binding energy of X_B should be the same for all structural phases. Similar suggestions have been made recently [42]. From the fitting, the binding energy of X_B is estimated to be $E_{b,B} = 21 \pm 3$ meV, which is consistent with the experimental reflectance where exciton B becomes weak after ~ 230 K [see Fig. 2(a)]. Remarkably, the binding energy agrees well with recent works on the $\text{CH}_3\text{NH}_3\text{PbBr}_3$ perovskite [19,44,45].

In the hydrogenlike model for Wannier-Mott excitons, the binding energy and the Bohr radius are expressed as $E_{b,j} = (m_j^*/m_0)(R_H/\epsilon_r^{*2})$ and $a_j = (m_0/m_j^*)\epsilon_r^* a_H$, respectively, where $j = A, B$, $R_H = 13.6$ eV is the Rydberg energy and $a_H = 0.053$ nm is the Bohr radius of the hydrogen atom. We use the effective mass as previously addressed as $m_B^* = 0.13m_0$ [39,45]. Hence, the effective dielectric constant is estimated to be $\epsilon_r^* = 9.18 \pm 0.66$. The Bohr radius is, therefore, $a_B = 3.74 \pm 0.27$ nm. Both ϵ_r^* and a_B values are in approximate agreement with previous literature reports [44,45].

Figure 3(c) shows the reflectance amplitude of exciton A . It does not change significantly with temperature, except for the phase transition, indicating that the binding energy $E_{b,A}$ is much larger than $k_B T$ at room temperature. In this case, the reflectance amplitude of the excitonic feature cannot be used to determine its binding energy. In order to overcome this issue, Fig. 3(d) shows the experimental reflectance (blue solid line) at $T = 10$ K along with the model combining the Elliot theory and the Kramers-Kronig relationship. The Elliot theory, which is normally used to explain the absorption of direct band-gap semiconductors, is converted to reflectance via the Kramers-Kronig transformation (see SM [48]). In our model, amplitudes of both excitons and the associated continuum bands are parametrized. The binding energy of X_A is variable, while that of X_B is set to 21 meV as calculated above. The exciton energies and linewidths are also fixed according to the aforementioned Lorentz model fitting in Fig. 2(a). The band-to-band transition (or continuum) energies are accordingly set as $E_j^{\text{b-b}} = E_{b,j} + E_{0,j}$ ($j = A, B$). The calculated curve, given by the pink dotted line, shows good agreement with the experimental reflectance, especially the excitonic features and the continuum band regions are well reproduced. The spectral band beyond ~ 2.4 eV does not follow, since higher energy bands are not included. By this computational method, the lower and upper bound of the binding energy of X_A are given as $E_{b,A} = 90 \pm 30$ meV (see Fig. S5 in SM [48]). The giant binding energy results in a large exciton mass evaluated as $m_A^* = (0.56 \pm 0.27)m_0$ and a small exciton Bohr radius calculated as $a_A = 0.87 \pm 0.48$ nm. These values are comparable to the large free-exciton binding energies and effective masses in oxide semiconductors such as CuO_2 [60,61] and ZnO [62–64]. The large $E_{b,A}$ makes free exciton A stable at room temperature and explains why it persists in the reflectance spectra up to 280 K [see Fig. 2(a)].

The calculated absorption coefficient as a function of energy is illustrated in Fig. 3(e). To further validate our approach, we perform another fitting on the reflectance spectrum at 10 K to a series of equally spaced and equally broadened Lorentz oscillators (see Fig. S6 and detailed fitting procedure in SM [48]). Both models provide similar spectral profiles and absorption coefficients ($\sim 10^5$ cm $^{-1}$). Additionally, they are in good agreement with the reported experimental absorption coefficient at comparable low temperature [39]. Therefore, we conclude the consistence of the computational approach using the combination of the Elliot theory and the Kramers-Kronig relationship.

In the absorption spectrum [see Fig. 3(e)], the free-exciton features A and B are reproduced at energies of ~ 2.244 eV and ~ 2.280 eV. They are represented by shaded areas under red and blue Lorentzian-shaped solid lines, respectively. The corresponding energies for band-to-band transitions are found at $E_B^{\text{b-b}} \sim 2.301$ eV and at $E_A^{\text{b-b}} \sim 2.334$ eV. Intriguingly, although X_A has lower energy than X_B , the band-to-band edge A lies slightly above the band-to-band edge B by ~ 33 meV owing to large $E_{b,A}$. Since the binding energies of both excitons are not affected by structural phases, the energy shifts with temperature of the continuum bands should follow those of excitons A and B . With increasing temperature from 10 K, it is expected that $E_B^{\text{b-b}}$ approaches $E_A^{\text{b-b}}$ to get close at approximately 140 K, just below the phase transition. At the high-temperature phase, $E_A^{\text{b-b}}$ red shifts further from $E_B^{\text{b-b}}$. The intricate energy landscape with nontrivial temperature dependence, including level crossing, may lead to a complicated optical response such as relaxation and recombination of photoexcited electron-hole pairs.

E. Discussion: Origins of the optical transitions

Next, we discuss the potential origins of X_A and X_B within the free-carrier representation for perovskites. Previous studies on $\text{CH}_3\text{NH}_3\text{PbBr}_3$ reported optical transitions behaving similarly to X_B [42–44]. In the orthorhombic phase, this exciton is widely accepted to originate from carriers at the Γ point of the Brillouin zone [23,30,31]. Nevertheless, none of the current theoretical calculations have suggested the existence of X_A . Relativistic Rashba effects have been considered, predicting the indirect nature of the fundamental band gap of organolead halide perovskites [34,36,37]. Two spin-polarized bands are separated evenly from the original high-symmetry point in both the conduction band (CB) and the valence band (VB). The stronger splitting expected at the CB leads to momentum mismatch (in k -space) which forbids direct transitions at the band edges. In this work, both X_A and X_B present clear signatures of direct transitions as revealed by pronounced oscillator strengths, large absorption coefficients, and strong photoluminescence emission. Recently, giant Rashba spin-splitting has been experimentally evaluated on $\text{CH}_3\text{NH}_3\text{PbBr}_3$ single crystal, giving an energy raise of 160 meV of the VB maximum with respect to the original maximum at the Γ point [38]. By noting the stronger Rashba effect at the CB, the energy difference between the direct transition (at Γ point) and the indirect transitions (at the spin-degenerated band edges) would be larger than 300 meV. However, the transition energies $E_A^{\text{b-b}}$ and $E_B^{\text{b-b}}$ differ by only ~ 33 meV, which is smaller by an

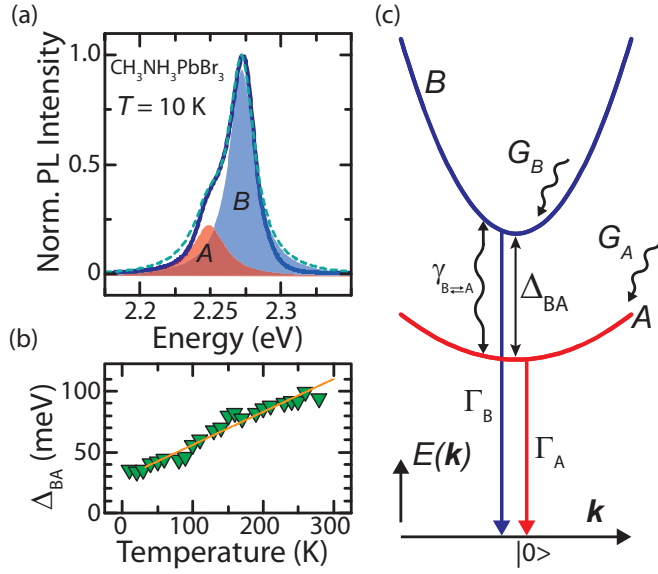


FIG. 4. (a) PL spectrum at 10 K (blue solid line) along with the fitting curve (green dashed line) using values from the reflectance modeling. The Lorentzian contributions from X_A and X_B to the total PL are represented by shaded red and blue areas, respectively. The intensity ratio is $I_B/I_A = 3.2$. (b) Energy splitting Δ_{BA} between excitonic levels B and A (green triangles) as a function of temperature. The orange solid line is a phenomenological linear fitting. (c) Schematic representation of free-exciton bands A and B . The symbols are used in the kinetic three-level model (see text).

order of magnitude. Therefore, the described picture about Rashba-induced indirect-direct transitions seems insufficient to explain the coexistence of excitons A and B .

We recall the different temperature responses of the exciton energies [see Fig. 3(a)]. Based on prior calculations, X_B is formed by carriers at Pb(s orbital)-Br(p orbital) antibonding and Pb(p orbital)-Br(p orbital) antibonding states in the VB and the CB, respectively [23,39,65,66]. On the other hand, the behavior of X_A to temperature is opposite and becomes stronger after 150 K. We suggest that the bonds between organic cations (CH_3NH_3^+) and halide anions (Br^-) may induce additional energy levels, from where the optical transition with energy $E_A^{\text{b-b}}$ arises. In this proposed scenario, one would expect that two (or multiple) excitons also exist in other lead halide perovskites (YMZ_3). For example, if the cation is replaced ($\text{Y}^+ = \text{FA}^+$ and Cs^+), the high-energy exciton (X_B) will behave similarly, while the behavior of the low-energy exciton (X_A) might change significantly. Whereas, if we alter the halide anion ($\text{Z}^- = \text{I}^-$, Cl^- , or mixed), both high- and low-energy excitons will be affected. Nevertheless, the precise origins of these excitons are not completely understood. A unified theoretical model, which can correlate our observations, spin-orbit coupling, Rashba effects and include the role of cations is needed to provide complete understanding of the complex band structures of the lead halide perovskite family.

F. Exciton dynamics: Photoluminescence intensity distribution

In Fig. 4(a), the experimental PL spectrum at 10 K (blue solid line) is fitted with two Lorentzians, in which the spectral position of the low-energy emission peak is fixed to the energy

of X_A obtained from the reflectance fitting. As seen, the fitting (green dashed line) matches well with the experimental data and reveals a counterintuitive behavior: emission from the high-energy exciton B (shaded blue area) has a contribution larger than that of the lowest-energy exciton A (shaded red area) to the total PL intensity. Indeed, the intensity ratio is $I_B/I_A \sim 3.2$. This ratio increases with increasing temperature (see Fig. S7 in SM [48] extracted from experimental data in Fig. 2(b)). Above 40 K, radiative recombination from excitonic band B dominates the light emission in $\text{CH}_3\text{NH}_3\text{PbBr}_3$. However, the asymmetric PL profile on the low-energy side reveals the weaker but nonzero contribution of X_A . This asymmetry is commonly observed in lead halide perovskites at room temperature [47,67,68] and is opposite to the normal intensity distribution in conventional semiconductors.

The PL intensity $I_j(E, T)$ resulting from excitonic recombination can be defined as $I_j(E, T) = N_j(E, T)\alpha_j(E, T)$ [56], where $N_j(E, T)$ and $\alpha_j(E, T)$ are population and absorption coefficients at the excitonic energy level X_j ($j = A, B$), respectively. The absorption coefficient is proportional to oscillator strength ($\alpha_j \propto F_j$) [69]. From the reflectance fitting, the oscillator strength of X_B is about ~ 3 times smaller than that of X_A (see Fig. 3(e) and Fig. S4 in SM [48]). Thus, oscillator strengths are not the reason for the striking PL distribution. Therefore, the population term needs to be considered.

In the case of noninteracting energy states, the thermal populations of photoexcited excitons on levels A and B depend on their energy splitting $\Delta_{BA}(T) = E_{0,B}(T) - E_{0,A}(T)$, whose temperature dependence is shown in Fig. 4(b). At 10 K, $\Delta_{BA} = 36$ meV is much larger than the thermal energy ($k_B T < 1$ meV), and this holds true at all temperatures. Such a large energy difference implies that the majority of excitons reside on the lowest-energy band A [see Fig. 4(c)]. Therefore, in this scenario, the contribution from the high-energy level B to the total PL intensity should be negligible. Nevertheless, we observe the opposite case: X_B dominates the PL spectrum.

To gain insight into the asymmetric PL profile, we employ the kinetic three-level model illustrated in Fig. 4(c) to describe the population of excitons A and B . The schematic energy diagram includes ground state $|0\rangle$, excitonic bands A (red curve) and B (blue curve), where the curvatures are proportional to the estimated effective masses m_A^* and m_B^* . The rate equations are given as

$$\frac{dN_A}{dt} = G_A - \Gamma_A N_A - \gamma_{A \rightarrow B} N_A + \gamma_{B \rightarrow A} N_B, \quad (3a)$$

$$\frac{dN_B}{dt} = G_B - \Gamma_B N_B - \gamma_{B \rightarrow A} N_B + \gamma_{A \rightarrow B} N_A, \quad (3b)$$

where G_A and G_B are generation rates of excitons at levels A and B , respectively, satisfying $G_A + G_B = 1$. Γ_A and Γ_B are radiative recombination rates of X_A and X_B , respectively, satisfying $\Gamma_A/\Gamma_B \approx F_A/F_B \sim 3$. Thermal coupling between A and B bands occurs via absorption or emission of phonons whose energies match Δ_{BA} . The nonradiative $A \rightarrow B$ and $B \rightarrow A$ relaxation rates are given by $\gamma_{A \rightarrow B} = \gamma_0 p(T)$ and $\gamma_{B \rightarrow A} = \gamma_0 [p(T) + 1]$, respectively, where γ_0 is the relaxation rate at zero-temperature, $p(T) = [\exp(\Delta_{BA}/k_B T) - 1]^{-1}$ is the Bose-Einstein phonon population at lattice temperature T .

The solution of Eq. (3) in the steady-state regime (i.e., $dN_{A(B)}/dt = 0$) yields the PL intensity ratio between X_A and X_B as

$$\frac{I_B}{I_A} = \frac{G_B + \gamma_{A \rightarrow B}/\Gamma_A}{G_A + \gamma_{B \rightarrow A}/\Gamma_B}. \quad (4)$$

The solution at 10 K can be further simplified by noting that $A \rightarrow B$ requires the absorption of the Δ_{BA} phonon mode. At 10 K, this process is negligible ($p \approx 0$), while phonon emission is always possible ($p + 1 \approx 1$). Therefore, exciton flow from $A \rightarrow B$ ($B \rightarrow A$) is forbidden (allowed). The relaxation rate $\gamma_{B \rightarrow A}$ is factorized in terms of Γ_B for a dimensional analysis.

To explain the asymmetric PL profile, we focus on the solutions of Eq. (4). Given the experimental intensity ratio $I_B/I_A \sim 3.2$, we find physical solutions for $\gamma_{B \rightarrow A}$ only if the generation rates of excitons A and B are inequivalent. Specifically, we find the minimum (maximum) threshold as $G_B = 0.76$ ($G_A = 0.24$) (see Fig. S8 in SM [48]). The generation rates imply that at least 76% of photogenerated carriers form free excitons at level B . The more electron-hole pairs are generated at the B band, the faster they relax from B to A . Considering the extreme case, where all excitons are created at level B (i.e., $G_B = 1$ and $G_A = 0$), $\gamma_{B \rightarrow A}$ reaches its maximum value at $\sim 0.3 \Gamma_B$. This means that nonradiative relaxation of excitons from $B \rightarrow A$ is much slower than direct radiative recombination from the high-energy level B .

We argue that exciton generation and relaxation pathways may depend on excitation wavelength. Here, under nonresonant excitation, electron-hole pairs are more efficiently created at level B . The inequivalent generation rates of excitons at A and B bands, together with a long relaxation time constant ($T_{B \rightarrow A} = 1/\gamma_{B \rightarrow A}$), explain the highly asymmetric profile of the low-temperature PL spectrum [see Fig. 4(a)].

Similar analyses have been done at higher temperatures from 20 K to 40 K. With increasing temperature, the intensity ratio I_B/I_A increases (see Fig. S7 in SM [48]). In this simplified model, the increment of I_B/I_A implies that the higher the temperature is, the more asymmetric the generation rates are and the slower the relaxation from B to A is. The increase of Δ_{BA} with increasing temperature also leads to the low relaxation rate $\gamma_{B \rightarrow A}$. Longer relaxation times at higher temperatures explain the stronger contribution of free excitons that radiatively recombine from level B to the PL spectrum. In order to describe the underlying physics behind the slow exciton dynamics in organolead halide perovskites, one may

need to consider Rashba effects, internal electric fields, and the dynamic disorder of the organic moieties [23,36].

IV. SUMMARY

We have shown that high-quality $\text{CH}_3\text{NH}_3\text{PbBr}_3$ single crystals provide a powerful platform to investigate the fundamental optical properties of lead halide perovskites. We have shown that two different classes of free-exciton transitions are responsible for the low- and high-temperature optical responses of the $\text{CH}_3\text{NH}_3\text{PbBr}_3$ single crystal. We find binding energies of 21 meV and 90 meV for high- and low-energy excitons, respectively. These results are in line with reconciling the wide range of exciton binding energies found in lead halide $\text{CH}_3\text{NH}_3\text{PbBr}_3$ perovskites. By using the hydrogenlike model, we supply important parameters for both exciton types that are useful for device application and nanostructure fabrication. Moreover, we explain the highly asymmetric PL intensity profile by using a simple three-level model. We find that under nonresonant photoexcitation, electron-hole pairs are more efficiently created at the high-energy band, and the subsequent nonradiative relaxation time to the low-energy level is longer than exciton radiative lifetimes. Since semiconducting lead halide perovskites share similar electronic band structures, our results could be extended to other compounds and be considered for future theoretical calculations. This work also provides a direct approach to investigate excitonic properties of other semiconductors.

ACKNOWLEDGMENTS

Q.H.X. gratefully acknowledges financial support from the Singapore National Research Foundation through an Investigatorship Award (Grant No. NRF-NRFI2015-03), the Competitive Research Program (Grants No. NRF-CRP-6-2010-2 and No. NRF-CRP14-2014-03), and the Singapore Ministry of Education via two AcRF Tier2 grants (Grants No. MOE2013-T2-1-049 and No. MOE2015-T2-1-047). Z.J.N. gratefully acknowledges financial support from the National Key Research Program (Grant No. 2016YFA0204000), the National Natural Science Foundation of China (Grants No. U1632118 and No. 21571129), the Shanghai Key Research Program (Grant No. 16JC1402100), and the Science and Technology Commission of Shanghai Municipality Project (Grant No. 16520720700).

T.T.H.D. and A.G.D.A. contributed equally to this work.

-
- [1] A. Kojima, K. Teshima, Y. Shirai, and T. Miyasaka, *J. Am. Chem. Soc.* **131**, 6050 (2009).
- [2] M. M. Lee, J. Teuscher, T. Miyasaka, T. N. Murakami, and H. J. Snaith, *Science* **338**, 643 (2012).
- [3] S. D. Stranks, G. E. Eperon, G. Grancini, C. Menelaou, M. J. Alcocer, T. Leijtens, L. M. Herz, A. Petrozza, and H. J. Snaith, *Science* **342**, 341 (2013).
- [4] Z. K. Tan, R. S. Moghaddam, M. L. Lai, P. Docampo, R. Higler, F. Deschler, M. Price, A. Sadhanala, L. M. Pazos, D. Credgington, F. Hanusch, T. Bein, H. J. Snaith, and R. H. Friend, *Nat. Nanotechnol.* **9**, 687 (2014).
- [5] H. Cho, S.-H. Jeong, M.-H. Park, Y.-H. Kim, C. Wolf, C.-L. Lee, J. H. Heo, A. Sadhanala, N. Myoung, S. Yoo, S. H. Im, R. H. Friend, and T.-W. Lee, *Science* **350**, 1222 (2015).
- [6] Y. Ling, Z. Yuan, Y. Tian, X. Wang, J. C. Wang, Y. Xin, K. Hanson, B. Ma, and H. Gao, *Adv. Mater.* **28**, 305 (2016).
- [7] E. Yassitepe, Z. Yang, O. Voznyy, Y. Kim, G. Walters, J. A. Castañeda, P. Kanjanaboos, M. Yuan, X. Gong, F. Fan, J. Pan, S. Hoogland, R. Comin, O. M. Bakr, L. A. Padilha, A. F. Nogueira, and E. H. Sargent, *Adv. Funct. Mater.* **26**, 8757 (2016).
- [8] J. Xing, F. Yan, Y. Zhao, S. Chen, H. Yu, Q. Zhang, R. Zeng, H. V. Demir, X. Sun, A. Huan, and Q. H. Xiong, *ACS Nano* **10**, 6623 (2016).
- [9] Q. Zhang, S. T. Ha, X. Liu, T. C. Sum, and Q. H. Xiong, *Nano Lett.* **14**, 5995 (2014).

- [10] G. Xing, N. Mathews, S. S. Lim, N. Yantara, X. Liu, D. Sabba, M. Grätzel, S. Mhaisalkar, and T. C. Sum, *Nat. Mater.* **13**, 476 (2014).
- [11] H. Zhu, Y. Fu, F. Meng, X. Wu, Z. Gong, Q. Ding, M. V. Gustafsson, M. T. Trinh, S. Jin, and X. Zhu, *Nat. Mater.* **14**, 636 (2015).
- [12] L. Dou, Y. M. Yang, J. You, Z. Hong, W.-H. Chang, G. Li, and Y. Yang, *Nat. Commun.* **5**, 5404 (2014).
- [13] Y. Fang, Q. Dong, Y. Shao, Y. Yuan, and J. Huang, *Nat. Photonics* **9**, 679 (2015).
- [14] B. R. Sutherland, A. K. Johnston, A. H. Ip, J. Xu, V. Adinolfi, P. Kanjanaboos, and E. H. Sargent, *ACS Photonics* **2**, 1117 (2015).
- [15] S. T. Ha, C. Shen, J. Zhang, and Q. H. Xiong, *Nat. Photonics* **10**, 115 (2015).
- [16] N. Kitazawa, Y. Watanabe, and Y. Nakamura, *J. Mater. Sci.* **37**, 3585 (2002).
- [17] J. H. Noh, S. H. Im, J. H. Heo, T. N. Mandal, and S. I. Seok, *Nano Lett.* **13**, 1764 (2013).
- [18] S. T. Ha, X. Liu, Q. Zhang, D. Giovanni, T. C. Sum, and Q. H. Xiong, *Adv. Opt. Mater.* **2**, 838 (2014).
- [19] R. Comin, G. Walters, E. S. Thibau, O. Voznyy, Z.-H. Lu, and E. H. Sargent, *J. Mater. Chem. C* **3**, 8839 (2015).
- [20] N. J. Jeon, J. H. Noh, W. S. Yang, Y. C. Kim, S. Ryu, J. Seo, and S. I. Seok, *Nature (London)* **517**, 476 (2015).
- [21] S.-T. Ha, R. Su, J. Xing, Q. Zhang, and Q. Xiong, *Chem. Sci.* **8**, 2522 (2017).
- [22] J. Even, L. Pedesseau, J.-M. Jancu, and C. Katan, *Phys. Status Solidi* **8**, 31 (2014).
- [23] J. Even, L. Pedesseau, C. Katan, M. Kepenekian, J.-S. Lauret, D. Saporì, and E. Deleporte, *J. Phys. Chem. C* **119**, 10161 (2015).
- [24] R. A. Jishi, O. B. Ta, and A. A. Sharif, *J. Phys. Chem. C* **118**, 28344 (2014).
- [25] Y. He and G. Galli, *Chem. Mater.* **26**, 5394 (2014).
- [26] K. Gesi, *Ferroelectrics* **203**, 249 (1997).
- [27] J. M. Frost and A. Walsh, *Acc. Chem. Res.* **49**, 528 (2016).
- [28] T. Wang, B. Daiber, J. M. Frost, S. Mann, E. C. Garnett, A. Walsh, and B. Ehrler, *Energy Environ. Sci.* **10**, 509 (2017).
- [29] N. Onoda-Yamamuro, T. Matsuo, and H. Suga, *J. Phys. Chem. Solids* **51**, 1383 (1990).
- [30] T. Baikie, Y. Fang, J. M. Kadro, M. Schreyer, F. Wei, S. G. Mhaisalkar, M. Graetzel, and T. J. White, *J. Mater. Chem. A* **1**, 5628 (2013).
- [31] W. Geng, L. Zhang, Y.-N. Zhang, W.-M. Lau, and L.-M. Liu, *J. Phys. Chem. C* **118**, 19565 (2014).
- [32] J. Even, L. Pedesseau, J. M. Jancu, and C. Katan, *J. Phys. Chem. Lett.* **4**, 2999 (2013).
- [33] F. Brivio, K. T. Butler, A. Walsh, and M. van Schilfgaarde, *Phys. Rev. B* **89**, 155204 (2014).
- [34] A. Amat, E. Mosconi, E. Ronca, C. Quarti, P. Umari, M. K. Nazeeruddin, M. Graetzel, and F. De Angelis, *Nano Lett.* **14**, 3608 (2014).
- [35] M. R. Filip and F. Giustino, *Phys. Rev. B* **90**, 245145 (2014).
- [36] P. Azarhoosh, S. McKechnie, J. M. Frost, A. Walsh, and M. van Schilfgaarde, *APL Mater.* **4**, 091501 (2016).
- [37] F. Zheng, L. Z. Tan, S. Liu, and A. M. Rappe, *Nano Lett.* **15**, 7794 (2015).
- [38] D. Niesner, M. Wilhelm, I. Levchuk, A. Osvet, S. Shrestha, M. Batentschuk, C. Brabec, and T. Fauster, *Phys. Rev. Lett.* **117**, 126401 (2016).
- [39] K. Tanaka, T. Takahashi, T. Ban, T. Kondo, K. Uchida, and N. Miura, *Solid State Commun.* **127**, 619 (2003).
- [40] V. D'Innocenzo, G. Grancini, M. J. Alcocer, A. R. S. Kandada, S. D. Stranks, M. M. Lee, G. Lanzani, H. J. Snaith, and A. Petrozza, *Nat. Commun.* **5**, 3586 (2014).
- [41] Q. Lin, A. Armin, R. C. R. Nagiri, P. L. Burn, and P. Meredith, *Nat. Photonics* **9**, 106 (2015).
- [42] N. Sestu, M. Cadelano, V. Sarritzu, F. Chen, D. Marongiu, R. Piras, M. Mainas, F. Quochi, M. Saba, A. Mura, and G. Bongiovanni, *J. Phys. Chem. Lett.* **6**, 4566 (2015).
- [43] H. Kunugita, T. Hashimoto, Y. Kiyota, Y. Udagawa, Y. Takeoka, Y. Nakamura, J. Sano, T. Matsushita, T. Kondo, T. Miyasaka, and K. Ema, *Chem. Lett.* **44**, 852 (2015).
- [44] J. Tilchin, D. N. Dirin, G. I. Maikov, A. Sashchiuk, M. V. Kovalenko, and E. Lifshitz, *ACS Nano* **10**, 6363 (2016).
- [45] K. Galkowski, A. Mitioglu, A. Miyata, P. Plochocka, O. Portugall, G. E. Eperon, J. T. W. Wang, T. Stergiopoulos, S. D. Stranks, H. J. Snaith, and R. J. Nicholas, *Energy Environ. Sci.* **9**, 962 (2016).
- [46] K. Zheng, Q. Zhu, M. Abdellah, M. E. Messing, W. Zhang, A. Generalov, Y. Niu, L. Ribaud, S. E. Canton, and T. Pullerits, *J. Phys. Chem. Lett.* **6**, 2969 (2015).
- [47] M. I. Saidaminov, A. L. Abdelhady, B. Murali, E. Alarousu, V. M. Burlakov, W. Peng, I. Dursun, L. Wang, Y. He, G. Maculan, A. Goriely, T. Wu, O. F. Mohammed, and O. M. Bakr, *Nat. Commun.* **6**, 7586 (2015).
- [48] See Supplemental Material at <http://link.aps.org/supplemental/10.1103/PhysRevB.96.075308> for sample characterization, additional analysis, optical measurements on the second sample, and details of the models used in the manuscript.
- [49] D. Shi, V. Adinolfi, R. Comin, M. Yuan, E. Alarousu, A. Buin, Y. Chen, S. Hoogland, A. Rothenberger, K. Katsiev, Y. Losovyj, X. Zhang, P. A. Dowben, O. F. Mohammed, E. H. Sargent, and O. M. Bakr, *Science* **347**, 519 (2015).
- [50] D. Sell, R. Dingle, S. Stokowski, and J. DiLorenzo, *Phys. Rev. Lett.* **27**, 1644 (1971).
- [51] J. Lagois and K. Hümmer, *Phys. Status Solidi B* **72**, 393 (1975).
- [52] G. Perna, V. Capozzi, S. Pagliara, M. Ambrico, and D. Lojaco, *Thin Solid Films* **387**, 208 (2001).
- [53] K. F. Mak, K. He, J. Shan, and T. F. Heinz, *Nat. Nanotechnol.* **7**, 494 (2012).
- [54] M. Fox, *Optical Properties of Solids*, Vol. 3 (Oxford University, London, 2010).
- [55] C. Kim, P. Lautenschlager, and M. Cardona, *Solid State Commun.* **59**, 797 (1986).
- [56] A. Zilli, M. De Luca, D. Tedeschi, H. A. Fonseka, A. Miriametro, H. H. Tan, C. Jagadish, M. Capizzi, and A. Polimeni, *ACS Nano* **9**, 4277 (2015).
- [57] C. V. Doorn, *Physica* **20**, 1155 (1954).
- [58] P. Dey, J. Paul, J. Bylsma, D. Karaiskaj, J. Luther, M. Beard, and A. Romero, *Solid State Commun.* **165**, 49 (2013).
- [59] Q. Zhang, R. Su, X. Liu, J. Xing, T. C. Sum, and Q. H. Xiong, *Adv. Funct. Mater.* **26**, 6238 (2016).
- [60] E. Gross, *Nuovo Cimento Suppl.* **3**, 672 (1956).
- [61] T. Kazimierzczuk, D. Fröhlich, S. Scheel, H. Stolz, and M. Bayer, *Nature (London)* **514**, 343 (2014).

- [62] D. C. Reynolds, D. C. Look, and B. Jogai, *Solid State Commun.* **99**, 873 (1996).
- [63] D. Bagnall, Y. Chen, Z. Zhu, T. Yao, S. Koyama, M. Y. Shen, and T. Goto, *Appl. Phys. Lett.* **70**, 2230 (1997).
- [64] T. Hanada, *Oxide and Nitride Semiconductors* (Springer, Berlin, 2009).
- [65] T. Umebayashi, K. Asai, T. Kondo, and A. Nakao, *Phys. Rev. B* **67**, 155405 (2003).
- [66] R. E. Brandt, V. Stevanović, D. S. Ginley, and T. Buonassisi, *MRS Commun.* **5**, 265 (2015).
- [67] M. S. Alias, I. Dursun, M. I. Saidaminov, E. M. Diallo, P. Mishra, T. K. Ng, O. M. Bakr, and B. S. Ooi, *Opt. Express* **24**, 16586 (2016).
- [68] G. Nedelcu, L. Protesescu, S. Yakunin, M. I. Bodnarchuk, M. J. Grotevent, and M. V. Kovalenko, *Nano Lett.* **15**, 5635 (2015).
- [69] G. Lanzani, *The Photophysics Behind Photovoltaics and Photonics* (Wiley & Sons, New York, 2012).